# Offset impact behaviour of bumper beam–longitudinal systems: numerical simulations

doi:10.1533/ijcr.2005.0106

S Kokkula[a], O S Hopperstad[b], O-G Lademo[b,c], T Berstad[c] and M Langseth[b]

[a] *FMC Kongsberg Subsea AS, Kirkegårdsveien 45, NO-3601 Kongsberg, Norway*
[b] *Structural Impact Laboratory (SIMLab), Department of Structural Engineering, Norwegian University of Science and Technology, NO-7491 Trondheim, Norway*
[c] *SINTEF Materials and Chemistry, Applied Mechanics and Corrosion, NO-7465 Trondheim, Norway*

**Abstract:** The paper presents the results from numerical simulations of bumper beam–longitudinal systems subjected to 40% offset impact loading. Numerical simulations were carried out with the non-linear finite element code LS-DYNA, searching for an efficient, numerically robust and accurate representation of the observed system behaviour. A comparative study of an industrial-like modelling procedure and another procedure incorporating a user-defined material model has been performed. In the latter procedure, the material model consists of state-of-the-art anisotropic plasticity, an isotropic strain and a strain-rate hardening rule as well as some ductile fracture criteria. Both shell and solid elements were utilized in discretizing the bumper beam–longitudinal set-up. Numerical crash results revealed good agreement with the experiments with respect to overall deformation mode and energy dissipation. The simulations were capable of giving relatively accurate prediction of the collapse mode found in the experimental tests, except for the bumper beam–longitudinal system with AA7003-T1 longitudinals. Sensitivity studies were performed considering both physical and numerical parameters. The physical parameters were strain-rate effects and the heat-affected zone, whereas the numerical parameter considered was adaptive meshing.

**Key words:** Modelling, explicit crash, energy dissipation, strain-rate, heat-affected zone, adaptive meshing.

## NOTATION

| | |
|---|---|
| $a_1, a_2, \ldots, a_8$ | dimensionless anisotropy parameters in *Yld2003* |
| *CFS*, *CFS** | critical fracture strain, with anisotropy |
| $\mathbf{C}$ | fourth-order tensor of elastic constants |
| $e$ | engineering strain |
| $e_{\mathrm{u}}$ | engineering strain corresponding to ultimate engineering stress |
| $f(\sigma, R)$ | yield function |
| $Q_{Ri}, C_{Ri}$ | material constants in the extended Voce rule |
| $r$ | *r*-value |
| $R$ | strain-hardening |
| $s_{\mathrm{f}}$ | engineering stress at fracture |
| $s_{\mathrm{u}}$ | ultimate engineering stress |
| $\alpha$ | angle |
| $\varepsilon$ | true strain |
| $\dot{\varepsilon}$ | true strain rate |
| $\dot{\bar{\varepsilon}}$ | effective plastic strain rate |
| $\dot{\varepsilon}_0, c$ | material parameters for the strain rate hardening model |
| $\boldsymbol{\varepsilon}, \boldsymbol{\varepsilon}^{\mathrm{e}}, \boldsymbol{\varepsilon}^{\mathrm{p}}$ | strain tensor, elastic and plastic |
| $\dot{\lambda}$ | plastic multiplier |
| $\sigma$ | true stress |
| $\sigma_0$ | yield stress |
| $\sigma_1$ | maximum principal stress |
| $\sigma_1', \sigma_2', \sigma_1'', \sigma_2''$ | principal values of transformed stresses |
| $\boldsymbol{\sigma}$ | stress tensor |

*Corresponding Author:*
S Kokkula
C/WO Riser System Engineering Group
FMC Kongsberg Subsea AS
Kirkegårdsveien 45, P.O. Box 1012, NO-3601 Kongsberg, Norway
Tel: 47-32-28-87-36; Fax: 47-32-28-67-50
E-mail: Satyanarayana.Kokkula@fks.fmcti.com

## INTRODUCTION

The need for computer crash simulations with high degrees of fidelity and robustness is becoming increasingly important for use in parametric studies and early design analysis. The numerical simulations also enable new design concepts to be evaluated where there is a need to establish an optimum design with an interaction between materials and structural forms. In order to reduce the time needed to develop a competitive new product, it is necessary to apply non-linear finite element (FE) analysis to design the manufacturing process and to evaluate the crashworthiness of the final component. Prior studies have shown that aluminium alloys used in the automotive applications have complex mechanical properties with anisotropic strength and ductility and that it may be necessary to use relatively complicated constitutive models to obtain the required accuracy in numerical analyses [1, 2]. On the other hand, efficient modelling of the system components is important.

The manufacturing of bumper beams from aluminium extrusions often involves a series of forming operations performed in the soft W-temper condition, and then artificial age hardening of the components to the peak hardness condition of the material. It is clear that for proper crash performance of the systems, the FE-model must rely upon the geometry obtained from a simulation of the process route, i.e. including simulation of all major forming operations. Moreover, the forming operations also result in an inhomogeneous evolution of some internal variables (among others the effective plastic strain) within the shaped components [1]. Lademo *et al.* [2] showed that plastic straining in W-temper results in significant change in the T6 work hardening curves. However, in industrial product development, process effects on material are not included. Instead, the homogeneous material properties of the final temper in its virgin/unformed state would be used even though the process effects may play a prominent role in the performance of the system in a crash. Traditional industrial modelling procedures for the numerical analyses of bumper beam systems include the most widely used material models, i.e. MAT-24 and MAT-103, in LS-DYNA [3], but these models do not support any attempt at including process effects on the material. For the accuracy and robustness of the analyses in general, it is, however, possible to include process effects into the numerical analyses and perform ‘process-based’ crash simulation.

Studying the impact behaviour of the bumper beam–longitudinal system is not trivial in the event of full-scale crash test of a car. Knowing the fact that frontal offset impacts are the most common accidental situations on roads, an experimental database was established for bumper beam–longitudinal systems subjected to 40% offset impact loading by Kokkula *et al.* [4]. This paper presents results from the numerical simulations that were carried out with the non-linear FE-code LS-DYNA [3]. The objective is to simulate the crash behaviour of the bumper beam–longitudinal systems at 40% offset impact and to compare the results with previously obtained experimental data [4].

From the experiments [4] on the bumper beam–longitudinal systems, it is observed that the major part of the deformation takes place as a combination of bending of the plate elements in the longitudinal members and bending of the bumper beam. The numerical model should be able to predict the collapse mode with a high level of certainty in order to ensure robust design.

## MATERIAL MODELLING

### General formulation

For the crash analyses of the bumper beam–longitudinal systems, reliability and efficiency are important criteria for the choice of a constitutive model for the materials in question. The following presents a summary of the equations of a constitutive model based upon Lademo *et al.* [1]. Small strains and rotations are assumed in the presentation, while large deformations are accounted in the co-rotational shell elements [5]. The strain tensor $\varepsilon$ is decomposed into elastic and plastic parts [6]

$$\boldsymbol{\varepsilon} = \boldsymbol{\varepsilon}^{\mathrm{e}} + \boldsymbol{\varepsilon}^{\mathrm{p}} \qquad [1]$$

where $\varepsilon^{\mathrm{e}}$ and $\varepsilon^{\mathrm{p}}$ are the elastic and plastic strain tensors. The relation between the stress tensor $\boldsymbol{\sigma}$ and the elastic strain tensor $\varepsilon^{\mathrm{e}}$ is defined as

$$\boldsymbol{\sigma} = \mathbf{C} : \boldsymbol{\varepsilon}^{\mathrm{e}} = \mathbf{C} : (\boldsymbol{\varepsilon} - \boldsymbol{\varepsilon}^{\mathrm{p}}) \qquad [2]$$

where $\mathbf{C}$ is the fourth-order tensor of elastic constants.

The yield function $f$, which defines the elastic domain in stress space, is expressed as

$$f = \bar{f}(\boldsymbol{\sigma}) - (\sigma_0 + R) \leq 0 \qquad [3]$$

where $\sigma_0$ is the reference yield stress and $R$ is the strain-hardening variable. The effective stress $\bar{\sigma}$ is defined by $\bar{\sigma} = \bar{f}(\boldsymbol{\sigma})$, while the convex function $\bar{f}$ is defined below. The strain hardening is given by [6]

$$R = \sum_{i=1}^{2} Q_{Ri}\,(1 - \exp(-C_{Ri}\bar{\varepsilon})) \qquad [4]$$

where $\bar{\varepsilon}$ is the accumulated plastic strain and $Q_{Ri}$ and $C_{Ri}$ are strain-hardening constants.

The associated flow rule defines the evolution of the plastic strain-rate tensor and the equivalent strain-rate as [6]

$$\dot{\varepsilon}^{\mathrm{p}} = \dot{\lambda}\frac{\partial f}{\partial \boldsymbol{\sigma}}, \quad \dot{\bar{\varepsilon}} = -\dot{\lambda}\frac{\partial f}{\partial R} \qquad [5]$$

where $\dot{\lambda} \geq 0$ is the plastic multiplier. The loading/unloading conditions are written in the Kuhn–Tucker form [5]

$$f \leq 0, \quad \dot{\lambda} \geq 0, \quad \dot{\lambda} f = 0 \qquad [6]$$

doi:10.1533/ijcr.2005.0106

These equations are used to define plastic loading and elastic unloading, while the consistency condition $\dot{f} = 0$ is utilized to determine the plastic multiplier $\dot{\lambda}$ during a plastic process.

### Strain-rate hardening

In order to account for rate dependency, the constitutive relation in the plastic domain can be written as [7]

$$\bar{\sigma} = \bar{f}(\boldsymbol{\sigma}) = (\sigma_0 + R(\bar{\varepsilon}))\left(1 + \frac{\dot{\bar{\varepsilon}}}{\dot{\varepsilon}_0}\right)^{c} \qquad [7]$$

where the exponents $c$ and $\dot{\varepsilon}_0$ are material parameters. For the rate-dependent material, Eq. (6) is substituted by

$$\left\langle \left(\frac{\bar{\sigma}}{(\sigma_0 + R(\bar{\varepsilon}))}\right)^{1/c} - 1 \right\rangle \dot{\varepsilon}_0 = \dot{\bar{\varepsilon}} \qquad [8]$$

where $\langle \cdots \rangle$ is the Macauley bracket, i.e. $\langle x \rangle = \max(x, 0)$.

### Yield criteria

Prior studies have shown that aluminium alloys used in automotive applications have complex mechanical properties with anisotropic strength and ductility and that it may be necessary to use relatively complicated constitutive models to obtain the required accuracy in the numerical analyses. In this work, the anisotropic yield criterion (*Yld2003*), that is proposed by Aretz [8], has been used for accurate and efficient representation of strong anisotropy in the materials [2]. The criterion contains eight anisotropy parameters that can be fitted to experimental data, and has a simple mathematical form that is also efficient for computational analysis [8]:

$$2\bar{f}^{\mathrm{m}} = |\sigma_1'|^{\mathrm{m}} + |\sigma_2'|^{\mathrm{m}} + |\sigma_1'' - \sigma_2''|^{\mathrm{m}} \qquad [9]$$

with the generalized principal stress transformations

$$\left.\begin{matrix}\sigma_1' \\ \sigma_2'\end{matrix}\right\} = \frac{a_8 \cdot \sigma_x + a_1 \cdot \sigma_y}{2} \pm \sqrt{\left(\frac{a_2 \cdot \sigma_x - a_3 \cdot \sigma_y}{2}\right)^2 + (a_4)^2 \cdot \sigma_{xy}\sigma_{yx}} \qquad [10]$$

and

$$\left.\begin{matrix}\sigma_1'' \\ \sigma_2''\end{matrix}\right\} = \frac{\sigma_x + \sigma_y}{2} \pm \sqrt{\left(\frac{a_5 \cdot \sigma_x - a_6 \cdot \sigma_y}{2}\right)^2 + (a_7)^2 \cdot \sigma_{xy}\sigma_{yx}} \qquad [11]$$

Here $a_1, a_2, \ldots, a_8$ are the dimensionless anisotropy parameters. These eight parameters can be uniquely found from eight experimental data points; the exponent $m$ can be taken as 6 for bcc and 8 for fcc materials [8].

### Fracture criterion

The fracture criterion employed in the current study is based on Yeh *et al.* [9]. They suggested that a critical fracture strain (*CFS*) can be used as the critical thickness strain (i.e. $\varepsilon_{\mathrm{cr}} = CFS$). *CFS* is defined as

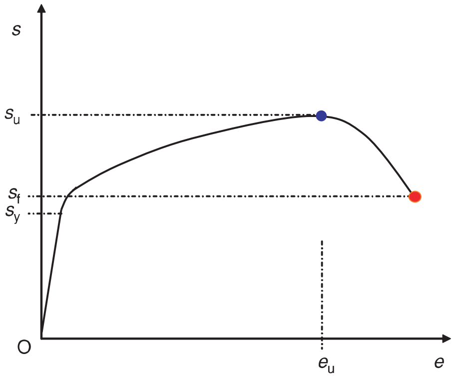

*Figure 1* Characteristic stress–strain curve under uniaxial loading for aluminium.

$$CFS = -\ln(1 - e_t) = -\ln\left[\left(1 - \frac{e_{\mathrm{u}}}{2}\right)\frac{s_{\mathrm{f}}}{s_{\mathrm{u}}}\right] \qquad [12]$$

where

$$e_t = \frac{e_{\mathrm{u}}}{2} + \left(1 - \frac{e_{\mathrm{u}}}{2}\right)\left(1 - \frac{s_{\mathrm{f}}}{s_{\mathrm{u}}}\right) \qquad [13]$$

where $s_{\mathrm{u}}$ is the ultimate engineering stress, $e_{\mathrm{u}}$ is the corresponding engineering strain and $s_{\mathrm{f}}$ is the engineering stress at fracture (see Figure 1). As the parameters are given from a standard tensile test, the *CFS* parameter is very easy to use and calibrate.

The following three assumptions were the basis for the development of *CFS* [9]:

$$\begin{array}{lll} \text{i)}\ \varepsilon_2 = \varepsilon_3 & \text{for} & e \le e_{\mathrm{u}} \\ \text{ii)}\ \varepsilon_2 = \text{constant} & \text{for} & e \ge e_{\mathrm{u}} \\ \text{iii)}\ \sigma_1 = \sigma_{1\mathrm{u}} & \text{for} & e \ge e_{\mathrm{u}} \end{array} \qquad [14]$$

In order to include anisotropy, the first assumption can be modified to

$$\varepsilon_2 = r\varepsilon_3 \quad \text{for} \quad e \le e_{\mathrm{u}} \qquad [15]$$

where $r$ is the $r$-value for the actual test specimen. By using these three assumptions, it can be shown that [10]

$$CFS^{*} = -\ln\left[(1 + e_{\mathrm{u}})^{-\frac{1}{1+r}} \cdot \frac{s_{\mathrm{f}}}{s_{\mathrm{u}}}\right] \qquad [16]$$

For an isotropic material ($r = 1$), the exponent $-1/(1 + r)$ equals $-\frac{1}{2}$. By expanding the term $(1 + e_{\mathrm{u}})^{-1/2}$ as a binomial series, assuming $|e_{\mathrm{u}}| = 1$, and retaining only the first two terms in the series, $CFS^{*}$ for an isotropic material can be approximated to *CFS* in Eq. (12). $CFS^{*}$ is easily calculated from the engineering stress–strain data and the $r$-values. $CFS^{*}$ was calculated for all repetitions, and the selected values for bumper beam and longitudinals in 0° direction are given in Table 1.

*Table 1* **Critical fracture values for bumper beam and longitudinal materials**

| Alloy | Bumper beam | Longitudinal | | |
|---|---|---|---|---|
| | AA7108 | AA7003 | | AA6060 |
| Temper | T6 | T79 | T1 | T1 |
| *CFS** parameter | 0.19 | 0.36 | 0.12 | 0.63 |

### Numerical aspects

The above-discussed constitutive and fracture model is implemented in LS-DYNA as a user-defined material model in the previous work ([2,11]) and is referred to here as MAT-41. As will be seen in the section 'Full-scale simulations of bumper beam–longitudinal systems', in addition to MAT-41, crash simulations of the bumper beam–longitudinal system are also performed with widely used industrial material models, i.e. MAT-24 (*piecewise linear isotropic plasticity*) and MAT-103 (*anisotropic viscoplastic*) (see Hallquist [3]). One difference between MAT-24 and MAT-103 is the hardening curve representation; in the former, a load curve with true stress–strain values is used directly or it can be given by eight-points, hence the name 'piecewise linear', while in the latter it is fitted with an extended Voce rule (Eq. (4)). Another difference is the choice of yield criterion, where MAT-24 is based on the von Mises yield criterion and MAT-103 is based on the yield criterion due to Hill [12]. Note, however, that the parameters of the Hill criterion have been chosen so that the yield surface is effectively the one represented by the von Mises yield criterion.

In the numerical simulations, when the fracture criterion is satisfied in one layer of a shell element this layer becomes inactive, i.e. the stress components in the layer are all taken to be equal to zero. When a user-defined number of integration points within an element have become inactive, the element is removed from the FE-model using the element erosion algorithm available in LS-DYNA [3]. This means that it is, in principle, possible to follow the evolution of a 'crack' through the plate elements. The fracture criterion is checked in all integration points in the elements for each time-step throughout the loading process.

In this study, five through-thickness integration points were used for the shell elements. In order to remove the element from the FE-model in the simulations, three integration points should reach the fracture criterion.

### Material parameters

Uniaxial tensile tests were performed in three material directions ($\alpha = 0^\circ$, $45^\circ$ and $90^\circ$) with respect to the extrusion direction, measuring force and length strain. For each experiment, true stress and true plastic strain were determined. Figure 2 shows the true stress versus plastic strain curves from uniaxial tensile tests along the extrusion direction, which is chosen as the reference direction.

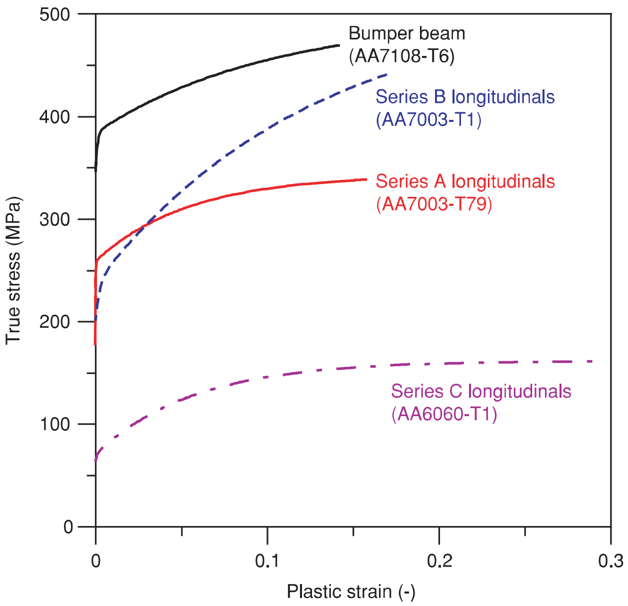

*Figure 2* Stress–strain curves identified from uniaxial tensile tests along extrusion direction for relevant alloy and temper conditions.

Table 2 summarizes the parameters obtained by fitting these results to the generalized Voce strain-hardening rule using a weighted least-square approach. In Table 3, the dimensionless anisotropy parameters for the Aretz yield criterion (*Yld2003*) have been identified based upon the same approach. The W-temper parameters shown in Tables 2 and 3 were used in the forming simulations (FE-model) of the bumper beam [14]. More details regarding the parameter identification can be found in Reyes *et al.* [7].

## FINITE ELEMENT MODEL OF BUMPER BEAM–LONGITUDINAL SYSTEM

The accuracy of any simulation depends on how accurately the modelling work has been carried out. Efforts were taken in constructing the numerical model of the bumper beam as similar as possible to reality. The bumper beam and all other components in the system were modelled and meshed in order to make a precise model using TrueGrid® pre-processor [13]. The same mesh size and constitutive model were used for both the forming and crash analyses. Anisotropy development due to pre-stretching is not included in the model, but no experiments have been performed to verify this assumption.

To achieve a bumper beam with geometric variations due to the forming operations, numerical simulations of all the forming operations were performed to obtain a rotary stretch-bent bumper beam. The generation of FE-model of the bumper beam following the industrial process route has been described in [14]. The geometry of the bumper beam obtained from numerical simulations was able to represent

*Table 2* **Hardening parameters for generalized Voce strain-hardening rule Eq. (4)**

| Alloy-temper | $\alpha$ | $\sigma_0$ (MPa) | $Q_{R1}$ (MPa) | $C_{R1}$ (–) | $Q_{R2}$ (MPa) | $C_{R2}$ (–) |
|---|---|---|---|---|---|---|
| AA7108-W | 0° | 41.9 | 37.7 | 2828 | 204 | 8.51 |
| AA7108-T6 | 0° | 347 | 37.0 | 1017 | 113 | 9.99 |
| AA7003-T79 | 0° | 239 | 20.4 | 4822 | 83.7 | 18.4 |
| AA7003-T1 | 0° | 202 | 35.3 | 455.9 | 276 | 7.89 |
| AA6060-T1 | 0° | 63.8 | 7.13 | 1403 | 91.0 | 17.4 |

*Table 3* **Dimensionless anisotropy parameters in Aretz yield criterion [8]**

| Alloy-temper | $a_1$ | $a_2$ | $a_3$ | $a_4$ | $a_5$ | $a_6$ | $a_7$ | $a_8$ |
|---|---|---|---|---|---|---|---|---|
| AA7108-W | 0.842 | 0.998 | 0.920 | 1.081 | 0.839 | 0.952 | 1.120 | 1.147 |
| AA7108-T6 | 0.839 | 0.979 | 0.969 | 1.087 | 0.855 | 0.979 | 1.103 | 1.161 |
| AA7003-T79 | 0.980 | 1.103 | 1.050 | 1.154 | 0.897 | 1.059 | 1.116 | 1.015 |
| AA7003-T1 | 0.924 | 1.061 | 1.001 | 1.229 | 0.874 | 1.035 | 1.131 | 1.069 |
| AA6060-T1 | 0.923 | 1.029 | 0.936 | 1.086 | 0.932 | 1.047 | 0.868 | 1.062 |

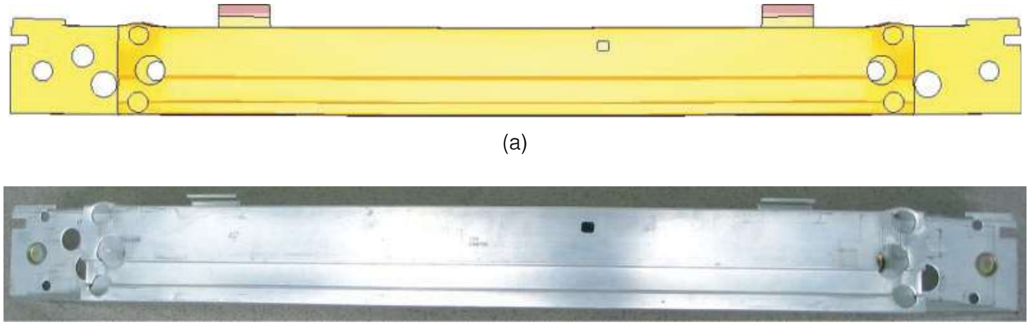
(a)

(b)

*Figure 3* (a) Virtual bumper beam from simulations (FE-model); (b) physical bumper beam.

the global behaviour satisfactorily with respect to the cross section and stretch-bent length. The full length of the stretch-bent bumper beam measured on the test specimen was 1388 mm, while that obtained from simulation was 1388.42 mm. The physical and virtual bumper beams are compared in Figure 3. The FE-model of the bumper only includes the thickness variations resulting from stretch-bending process.

All the components were assembled with respect to the location of the stretch-bent bumper beam. The impactor was positioned carefully so that it did not penetrate into the upper flange of the bumper beam. The test set-up of the FE-model after the assembly of all components that are ready for crash simulation is shown in Figure 4. Modelling aspects for the various parts of the bumper beam–longitudinal system are summarized in Table 4.

For the various contact conditions in the system, different types of contact algorithms were employed to ensure that the minimum penetration of parts occurred which did not result in any numerical problems. The contact types employed are summarized in Table 5. In the tests, the bumper beam was connected to the longitudinals via the interface plates using a bolted connection, whereas the longitudinals were connected to the interface plate through MIG welding. The modelling of this bolted connection is clearly shown in Figure 5. The connections used in the simulations are summarized in Table 6.

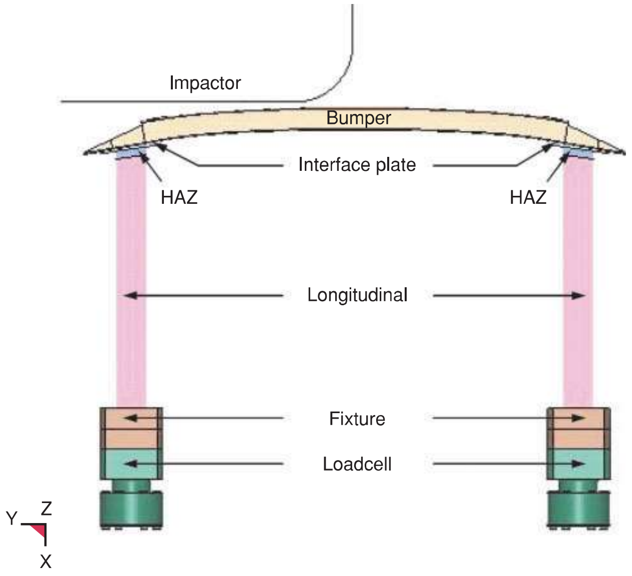

*Figure 4* The FE-model of the bumper beam–longitudinal system.

*Table 4* **Modelling aspects of components used in crash analysis of bumper beam–longitudinal system**

| Modelling aspects | Description |
|---|---|
| Bumper beam AA7108 | |
| Element type | Quadrilateral (Belytschko–Lin–Tsay shell) (default) |
| Integration points | 1 in-plane and 5 through-thickness |
| Hourglass control | Stiffness form |
| Number of elements | 19,154 |
| Element size (approximately) | $5.0 \times 5.0\ \text{mm}^2$ |
| Material strain-rate effects | Neglected |
| Geometrical imperfections | None |
| Total mass | 4.5 kg |
| Longitudinal and HAZ | |
| Element type | Quadrilateral, Belytschko–Lin–Tsay shell (default) |
| Integration points | 1 in-plane and 5 through-thickness |
| Hourglass control | Stiffness form |
| Number of elements | Longitudinal: 8448, HAZ: 264 |
| Element size (approximately) | $5.0 \times 5.0\ \text{mm}^2$ |
| Effective extrusion length | Longitudinal: 630 mm, HAZ width: 20 mm |
| Material strain-rate effects | Neglected |
| Geometrical imperfections | None |
| Nodal constraints | All degrees of freedom free – lower end nodes are merged with the fixture, upper end nodes are merged with interface plate |
| Total mass | 2 kg |
| Fixture and loadcell (including bottom plate and bolts) | |
| Element type | Hexahedron brick (default) |
| Integration points | 1 |
| Hourglass control | Full Flanagan–Belytschko stiffness form with exact volume integration |
| Material models | MAT-3, (load cell and bolts) elastic–plastic, bilinear kinematic hardening. 210,000 MPa, tangential modulus 700 MPa, yield stress 600 MPa, density 7850 kg/m$^3$, Poisson's ratio 0.33<br>MAT-20, (fixture bottom plate) rigid body |
| Number of elements | 78,016 – load cell, 1368 – bottom plate, 2784 – bolts, 414 – fixture |
| Element size (approximately) | min: 1 mm, max: 5 mm (load cell)<br>min: 5.1 mm, max: 100 mm (fixture) |
| Material strain-rate effects | Neglected |
| Nodal constraints | Fixture, load cell and bolts: all degrees of freedom free<br>Bottom plate: all degrees of freedom are constrained |
| Total mass | Load cell (including bottom plate and bolts): 48.378 kg, Fixture: 40 kg |
| Interface plate | |
| Element type | Quadrilateral, Belytschko–Lin–Tsay shell (default) |
| Integration points | 1 in-plane and 5 through-thickness |
| Hourglass control | Stiffness form |
| Number of elements | 910 |
| Element size (approximately) | $5.0 \times 5.0\ \text{mm}^2$ |
| Material models | MAT-103 |
| Material strain-rate effects | Neglected |
| Nodal constraints | All degrees of freedom free – nodes are merged with HAZ |
| Total mass | 0.289 kg |
| Impactor | |
| Element type | Not applicable |
| Integration points | Not applicable |
| Number of elements | 1210 |
| Element size (approximately) | min: 7.5 mm, max: 13.5 mm |
| Material models | MAT-20, rigid body |
| Nodal constraints | All degrees of freedom are constrained, except the $x$-direction translation degree is set free and all the nodes were given an initial impact velocity |
| Total mass | 794 kg |

doi:10.1533/ijcr.2005.0106

*Table 5* **Modelling of contact in the crash analysis**

| Modelling aspects | Description |
|---|---|
| Bumper beam (S) | Automatic single surface, penalty based, friction coefficient 0.2 |
| Longitudinal and HAZ (S) | Automatic single surface, penalty based, friction coefficient 0.2 |
| Impactor (M) – Bumper beam (S) | Automatic nodes to surface, penalty based, friction coefficient 0.6 |
| Interface plate (M) – Bumper beam (S) | Automatic nodes to surface, penalty based, friction coefficient 0.0 |
| Interface plate (M) – Longitudinal (S) | Automatic surface to surface, penalty based, friction coefficient 0.0 |

S stands for slave set nodes and M for master set nodes.

*Table 6* **Modelling of connection in the crash analysis**

| Modelling aspects | Description |
|---|---|
| Bumper beam and interface plate | Bolt connection was used between the bumper beam lower flange and interface plate in the test. In the numerical simulations, this was done as follows: in each bolting position, four elements are made as rigid in bumper beam and in the interface plate. The same rigid material is used for both bumper beam and interface plate elements for the same bolt, but different rigid material in the different bolt locations, so that the different bolts are not connected to each other (see Figure 5) |
| Longitudinal and interface plate | The nodes in the HAZ of the longitudinal were merged with the nodes of interface plate |

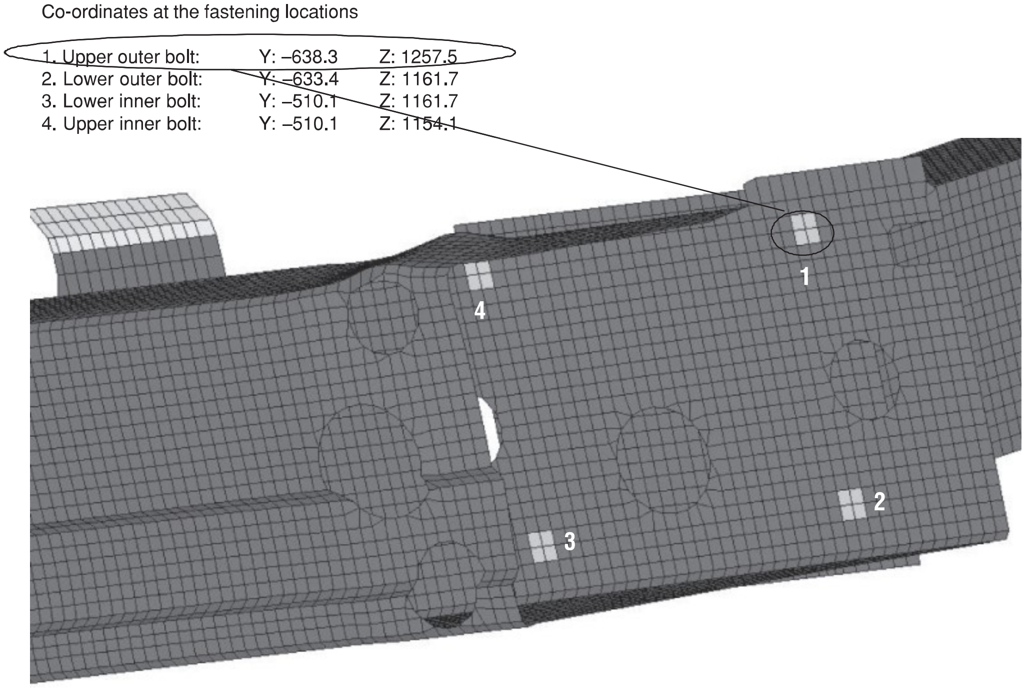

Co-ordinates at the fastening locations

| | | |
|---|---|---|
| 1. Upper outer bolt: | Y: –638.3 | Z: 1257.5 |
| 2. Lower outer bolt: | Y: –633.4 | Z: 1161.7 |
| 3. Lower inner bolt: | Y: –510.1 | Z: 1161.7 |
| 4. Upper inner bolt: | Y: –510.1 | Z: 1154.1 |

*Figure 5* Modelling of bolted connection between the bumper beam lower flange and the interface plate.

The interface plate and the longitudinal were connected by welding. Thus, it was assumed that a part of the extruded longitudinal member and the interface plate had a heat-affected zone (HAZ). In the numerical model the longitudinal and the interface plate, the HAZ was modelled with an assumed length of 20 mm [14] (see Figure 4). The reduced true stress–strain curve used for the HAZ is shown in Figure 6. This is the same as that used to represent the base material (longitudinal) but with 30% shift in the true stress–strain curve according to Eurocode 9 specifications [15]. In the simulations, the failure criterion was not considered for the HAZ elements.

## EXPLICIT SIMULATIONS

Only explicit crash simulations were performed in this study. However, implicit dynamic simulations of the bumper beam–longitudinal systems can also be performed but the convergence becomes critical due to the number of contact definitions, which requires a lot of simulation time [16]. The simulations were performed on a single

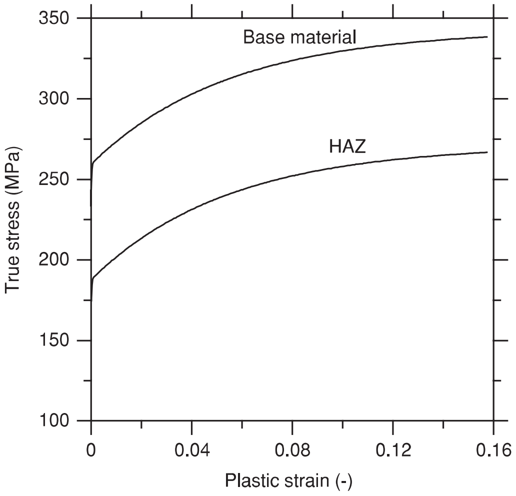

*Figure 6* Stress–strain curves used in the base material and HAZ.

Linux processor. LS-DYNA uses a central difference operator for time integration, requiring a limitation on the time-step size. In order to obtain numerical stability during the crash simulations, the time-step size is typically in the order of 1 $\mu$s. All the simulations were executed with a variable time step. It is also possible to execute the simulations with a fixed time step, which generally has the potential of yielding large errors in analyses including inertia effect. For the present bumper beam–longitudinal system in Figure 4, the loadcells were also modelled. Because of the fine mesh in the loadcells, the time-step size was often controlled by these elements and thus an initial time-step size of 0.168 $\mu$s was generated by LS-DYNA.

## FULL-SCALE SIMULATIONS OF BUMPER BEAM–LONGITUDINAL SYSTEMS

The experimental results in [4] showed that the energy absorption was found to depend on the yield strength, temper condition (and thus strain-hardening of the material) and the collapse mode of the longitudinals. The main objective here was to investigate the ability of the non-linear FE-code LS-DYNA [3] to predict the response, and the main focus was placed on accurate prediction of the observed system behaviour with respect to force–deformation characteristics and fracture modes. The alloy and temper used in different test series are given in Table 7.

In order to check the influence of the choice of yield criterion, simulations were performed with the most widely used industrial material models in LS- DYNA, i.e. MAT-24 and MAT-103, as well as with MAT-41. The simulations that were performed in this study are summarized in Table 8. For each test series, the simulation results are compared with the experimental results.

*Table 7* **Materials for the different test series and bumper beam**

| Test series | Longitudinals | Impact velocity (m/s) |
|---|---|---|
| A | AA7003-T79 | 10 |
| B | AA7003-T1 | 10 |
| C | AA6060-T1 | 10 |
| Bumper beam in alloy AA7108-T6 | | |

*Table 8* **Summary of simulations performed with different material models**

| Test series | Material models used |
|---|---|
| A | MAT-24 [3], MAT-103 [3], MAT-41, MAT-41(*CFS**) |
| B | MAT-41, MAT-41(*CFS**) |
| C | MAT-41, MAT-41(*CFS**) |

The difference between the analyses denoted by MAT-41 and MAT-41(*CFS**) is that the former analyses are run without an activated fracture criterion and the latter are run with critical thickness strain fracture criterion, see the section ‘Fracture criterion’ . It is possible to use a fracture criterion in MAT-24 based on the effective plastic strain [3]. However, no attempt was made to use this fracture criterion in connection with MAT-24. Further, when using MAT-103 the ability to represent the planar anisotropy using the quadratic yield criterion was not exploited.

### Force–deformation

In the simulations, the impact energy was converted to plastic work by bending and stretching the bumper beam as well as crushing the longitudinal at the impacted end and also bending of the non-impacted longitudinal.

#### *Test series A*

For test series A, the force–deformation and mean force–deformation plots are shown in Figure 7. One can clearly note that the response of the bumper beam–longitudinal system predicted by MAT-24 and MAT-103 material models is slightly ‘stiffer’ than what is predicted by MAT-41 and MAT-41(*CFS**). The main difference between MAT-24 and MAT-103 is the hardening curve representation; in the former model the measured true stress–stain values were used, while in the latter the measured values were fitted with a five-parameter Voce strain-hardening rule (see Eq. (4)). Obviously, this can overpredict the energy that can be dissipated, since actual materials will fail at some deformation. As will be seen later in this section, the material models MAT-24 and MAT-103 overpredicted the energy dissipation partly due to lack of a fracture criterion and anisotropy.

The permanent deformation of the bumper beam–longitudinal system in test series A varied from 412 to 440 mm with nine fully developed lobes in the impacted longitudinal [4]. The predicted permanent deformation, energy dissipation, number of lobes developed and the CPU time consumed for running the simulation when using

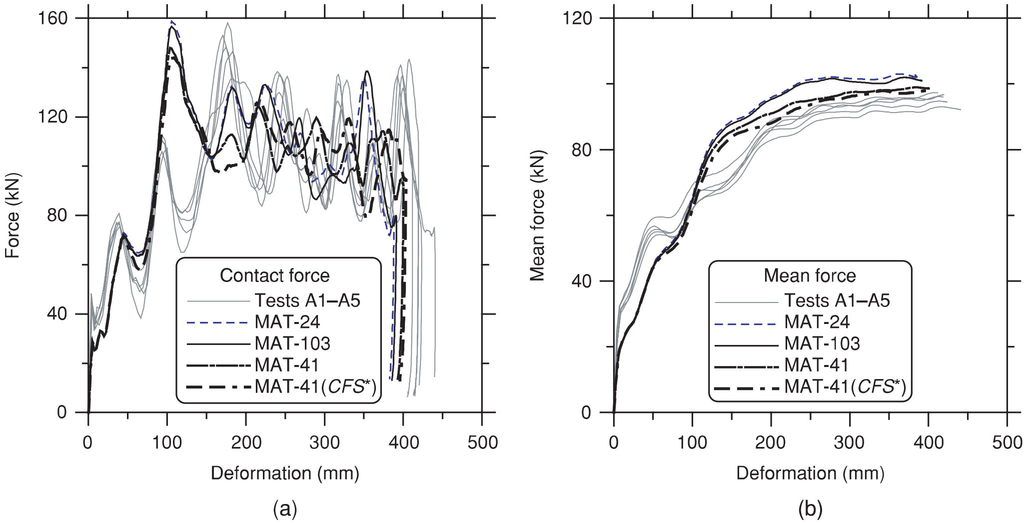

*Figure 7* Comparison of (a) force–deformation and (b) mean force–deformation plots from the tests and simulations with different material models for test series A.

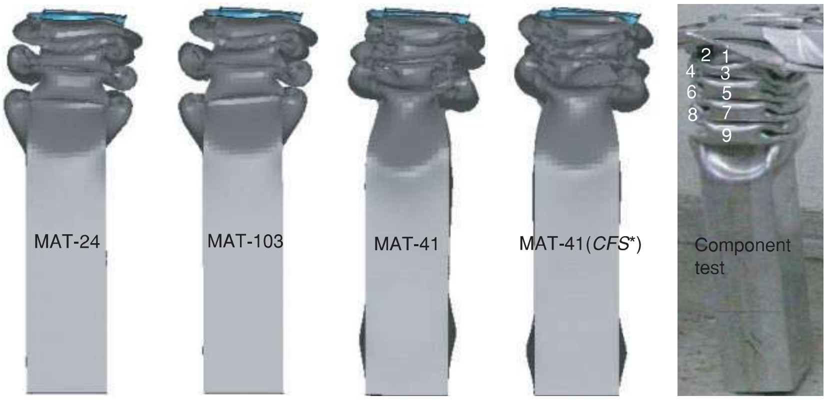

*Figure 8* Development of lobes in the impacted longitudinal in simulations and test.

*Table 9* **Predicted permanent deformation, energy dissipated and number of lobes from simulations when using different material models for test series A**

| Material model | Permanent deformation (mm) | Energy dissipated (kJ) | Number of lobes | CPU time consumption (h) |
|---|---|---|---|---|
| MAT-24 | 395 | 38.32 | 6 | 53 |
| MAT-103 | 400 | 38.38 | 6 | 54 |
| MAT-41 | 400 | 38.17 | 7 | 74 |
| MAT-41(*CFS**) | 405 | 38.01 | 7 | 77 |

different material models are given in Table 9. The number of lobes developed in the impacted longitudinal in the simulations when using different material models is compared to the one observed in the experimental tests in Figure 8. The number of lobes developed in the impacted longitudinal was three less with MAT-24 and MAT-103 models, whereas it was two less with MAT-41. However, the lobes developed with MAT-41 were rather a mixed mode, while a progressive mode was observed in the tests. The underprediction of lobes in the simulations may be due to the mesh size and also the lack of modelling of the initial imperfections in the extruded member.

The impacted longitudinal started to buckle at its clamped end when using MAT-41; this can be clearly seen in Figure 8. However, no such buckle was observed in the tests. One should also remember that the nodes between the longitudinal and the fixture (modelled as a rigid body, see the section 'Finite element model of bumper beam–longitudinal system') were merged in the FE-model. In these tests, the longitudinals were fixed inside a rectangular slot in the fixture, using a sliding block mechanism (see Figure 6 of [4]).

For the same amount of deformation, the predicted dissipated energy using the current material models is higher

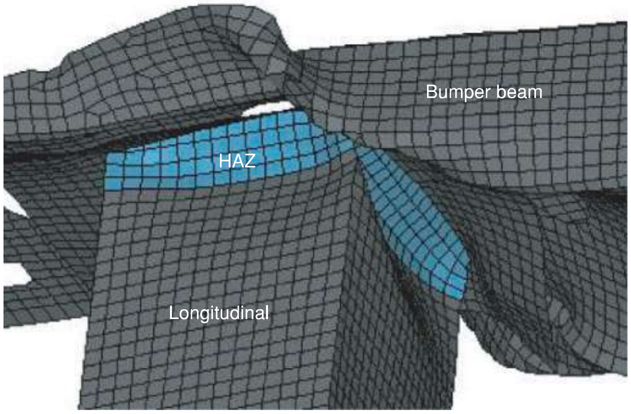

*Figure 9* A close view of the first buckle developed in the impacted longitudinal of test series A.

than that from tests (Figure 7). The predicted mean force is close to the tests when using the MAT-41(*CFS**); the predicted permanent deformation, however, is slightly higher than that of MAT-24 and MAT-103. From the above, it is clear that there is some influence from the chosen material model, and thus the yield criterion, on the predicted behaviour of the bumper beam-longtudinal system. The increase in computational time when using MAT-41 and MAT-41(*CFS**) was due to the complex nature of the yield criterion and also the use of a fracture criterion.

From the force–deformation curves (Figure 7(a)), several crash events can be identified. The force level in the initial stages of crushing corresponds to the collapse of the bumper beam cross section. After the collapse of the bumper beam cross section (at a displacement of 60 mm) at the impacted end, the force level in the simulations is governed by the initiation of the folding mechanism in the impacted longitudinal giving a high peak load caused by the buckling of the longitudinal. Figure 9 shows the development of the first buckle in the impacted longitudinal. The figure clearly shows that an *asymmetric* folding mode (usually called an *extensional* mode) developed as the first buckle, because the two adjacent walls of the impacted longitudinal buckled inwardly. However, in the tests [4] an *axisymmetric* folding mode was observed for the first buckle.

### *Test series B*

Test series B simulations were performed only with the MAT-41 model with and without the *CFS** fracture criterion. For modelling the HAZ, a 30% shift (decrease) in the true stress–strain curve of the base material was used, as was done in test series A. In the experiments [4], it was observed that the crashboxes on the reaction wall were activated. The activation was mainly due to the unacceptable failure modes in the impacted longitudinal. However, the simulations were run up to the termination time at which the impactor velocity became zero.

The force–deformation and mean force–deformation curves obtained from the numerical simulations, with and without a failure criterion, are plotted against the test results in Figure 10. During the initial stages of the crushing process, i.e. the collapse of the bumper beam cross section and initiation of buckling in the impacted longitudinal, the force–deformation curves from the simulations followed the experimental curves of test specimens B1 and B2. This corresponds to a deformation of 100 mm (see Figure 10(a)). However, the peak force predicted in the numerical simulations was much higher than that of the tests, and is related to the development of the first buckle in the impacted longitudinal. The first buckle developed was similar to that observed in series A simulation as in the previous section.

In the simulations, a progressive folding mode developed in the impacted longitudinal. One can easily note this from the oscillations of the curves around a mean value, after the maximum peak in the force–deformation curves (Figure 10(a)). The figure clearly depicts that the simulations terminated at a deformation of about 400 mm. At

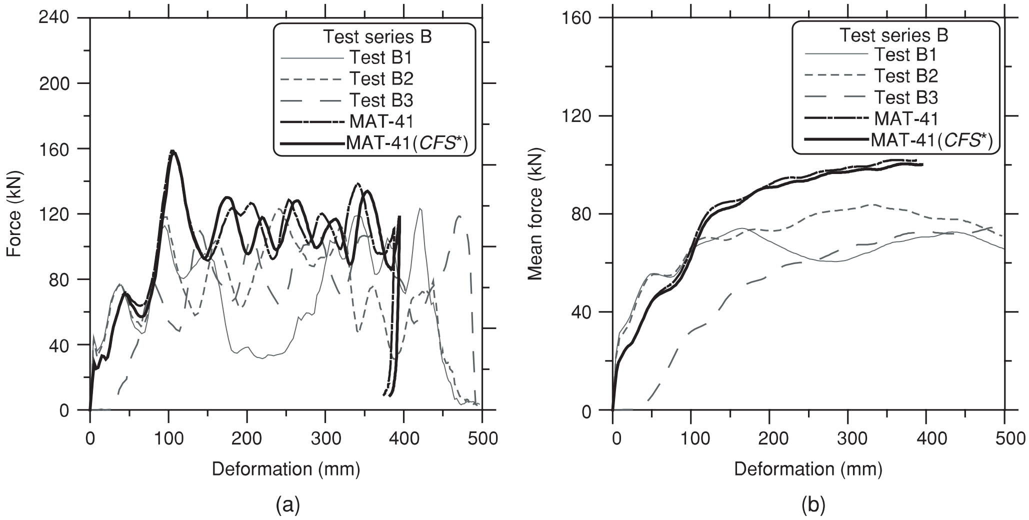

(a) (b)

*Figure 10* Comparison of (a) force–deformation and (b) mean force–deformation plots from the tests and simulations for test series B.

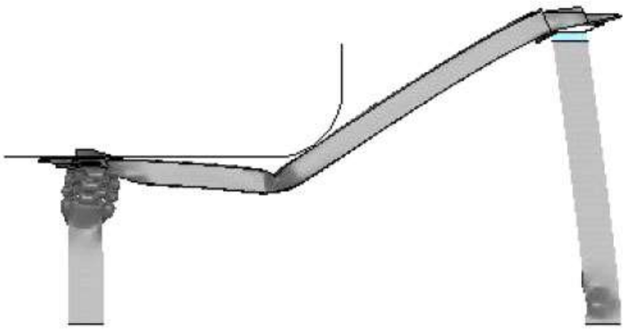

*Figure 11* Final deformation shape of series B bumper beam-longitudinal system.

this deformation, the impact energy was absorbed by the bumper beam–longitudinal system. This indicates that if the unacceptable failure in the impacted longitudinal had not prevailed, the longitudinal might have deformed progressively up to the deformation predicted in the simulations (i.e. 400 mm). From the mean force–deformation curves in Figure 10(b), one can note that there is no difference between the simulation results with and without a fracture criterion. However, the predicted mean force is significantly higher than in the tests. In the experiments of test series B [4], a transition from progressive buckling to a global bending mode was observed in the impacted longitudinal for test specimens B1 and B3, whereas a progressive folding mode was observed for test specimen B2.

Simulations were also performed without the HAZ in order to predict the deformation and fracture modes as in the tests; no improvement was observed, and hence they are not reported. It can be said that the simulations failed to predict the deformation and fracture modes that were observed in the tests (see Figure 16 in [4] and Figure 11).

### *Test series C*

For test series C, simulations were performed with the MAT-41 model with and without the *CFS** fracture criterion. From the high-speed video recordings, it was observed that the crashboxes on the reaction wall were activated in all the three parallels [4]. To represent this activation in the numerical simulations, the key word *TERMINATION_BODY available in LS-DYNA [3] was used. With the use of this keyword, the impactor was stopped at the desired displacement.

When performing the simulations of test series C, the HAZ was not modelled. It was observed from the simulations that when the HAZ was modelled (as in test series A and B) the bumper beam–longitudinal system ran into a global buckling mode. Hence, the HAZ was avoided to obtain the stable behaviour as in the tests. The force–deformation and mean force–deformation curves from the experiments and simulations with and without the fracture criterion are shown in Figure 12.

As with the tests, the longitudinal at the impacted end started to buckle before the complete collapse of the bumper beam cross section. With the increase in force, the web of the bumper beam buckled outwardly at the impacted end and simultaneously a plastic hinge developed in its mid-section. This can be noted from the first peak in the force–deformation plots (Figure 12(a)), at a deformation of about 50 mm. A progressive folding mode developed in the impacted longitudinal with further increase in the impact force. The oscillations in the force–deformation plots around the mean value are due to the formation of new lobes in the impacted longitudinal.

The mean force–deformation plots in Figure 12(b) clearly show that there is no difference between the curves obtained from simulations with and without fracture, but the predicted mean force level is somewhat too low. The lower mean force level recorded in the simulations may be

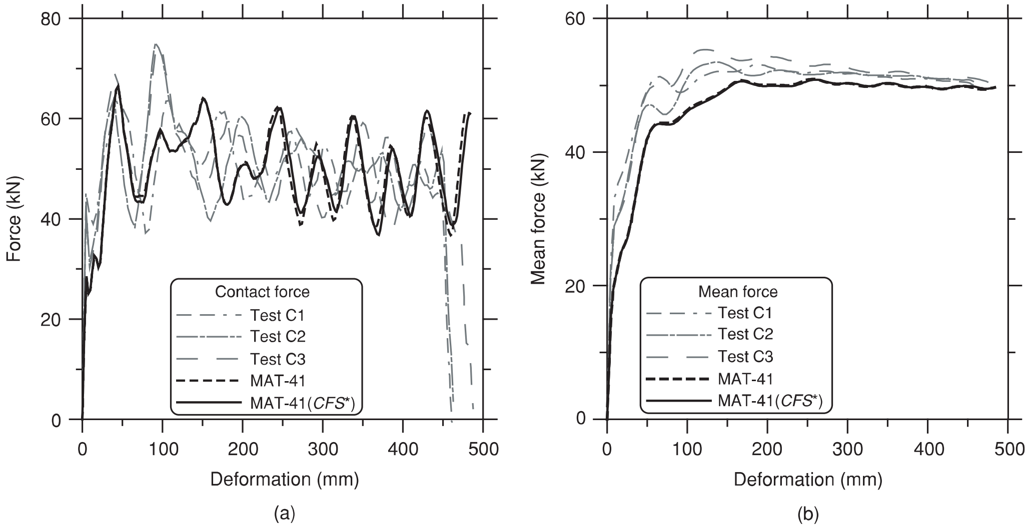

*Figure 12* Comparison of (a) force–deformation and (b) mean force–deformation plots from the tests and simulations for test series C.


(a)

(b)

(c)

*Figure 13* Comparison of permanent deformation shapes of test specimen A1 [4] and that obtained from simulation with MAT-41(*CFS**).

due to strain-rate effects that have been ignored. As will be seen in the section 'Strain-rate', the predicted mean force level is close to the experiments when the strain-rate effects are considered in the simulations. In the experiments, it was observed that there were no significant fracture events in the bumper beam–longitudinal systems in accordance with the simulations. Thus the predicted curves with and without fracture criterion are on top of each other.

### Deformation shape

The fidelity and accuracy of the simulations can be studied in several ways. Firstly, the general deformations at the impact regions were compared visually to the images captured with the high-speed camera. Secondly, the permanent deformations were compared.

Deformation shapes from the simulation and the experiments for test series A are compared in Figure 13. It is clear from Figure 13(a) that the non-impacted longitudinal in the simulations had a more dominant local buckle nearby its clamped end than in the tests. The probable reason, as mentioned earlier, is the merging of nodes between the longitudinal and the fixture. The bending failure in the mid-section of the bumper beam is compared in Figure 13(b), and is poorly predicted in the simulations. In Figure 13(c), it is seen that neither the through-thickness shear crack at the cut-out region of the non-impacted end of the bumper beam nor the propagating tearing crack at the intersection between the lower flange and the web is predicted in the simulation.

From the post-crash test specimens of test series A, a considerable number of failure zones have been observed in the folds of the impacted longitudinal. A direct view of the geometry does not reveal direct erosion of any element in the same zones. However, element deletion occurs only when the three through-thickness integration points reach the fracture criterion. The elements that reached the fracture criterion in different through-thickness integration points for the impacted longitudinal are shown in Figure 14. Be aware that in the figure the deformation is greatly reduced to show the elements. Further, the HAZ is not included in the figure. If one considers that the first integration point belongs to the outer layer then the fifth integration point represents the inner layer of the element or vice-versa. The elements in which the integration point reached the fracture criterion are denoted by light colour

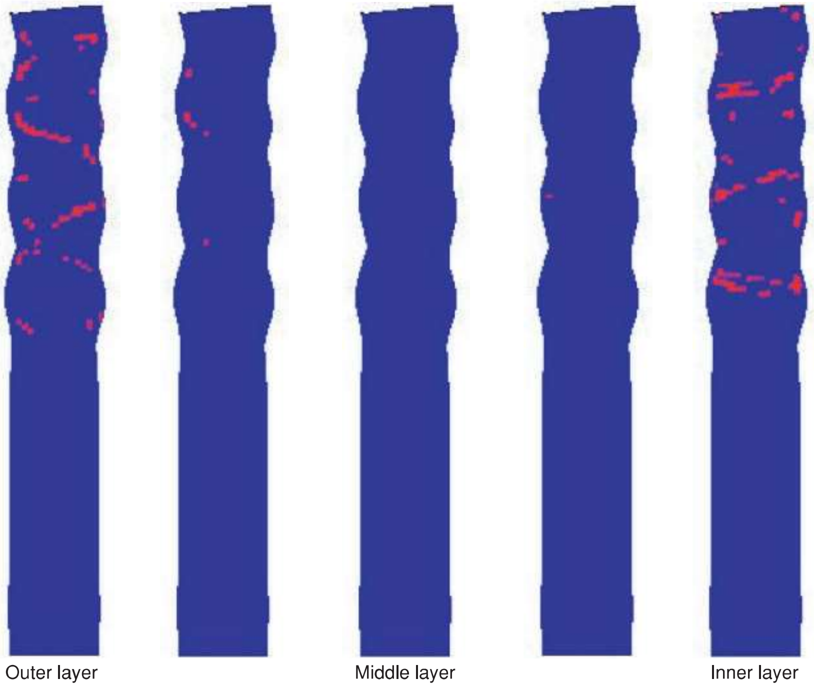

*Figure 14* Elements that reached the critical thickness strain fracture criterion (*CFS**) in the impacted longitudinal for each integration point for test series A in the simulation.

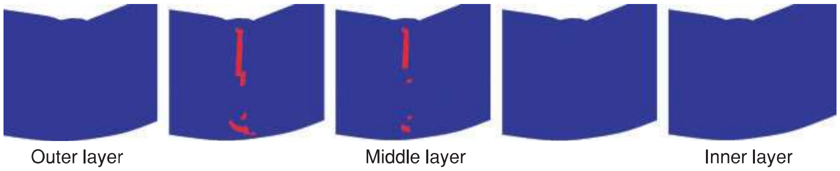

*Figure 15* Elements that reached the critical thickness strain fracture criterion (*CFS**) in the bumper beam for each integration point for test series A in the simulation.

(red). Thus, the surface cracks that are observed in the folds of the impacted longitudinal can be adequately represented by these failed integration points. However, in none of the elements, the third through-thickness integration point reached the fracture criterion and hence no element was deleted.

The bending failure in the folded elements of the bumper beam in the simulations is shown in Figure 15. The elements in light colour (red) represent the integration points that reached the critical thickness strain fracture criterion. As in the impacted longitudinal, only two integration points reached the fracture criterion and thus no elements were removed.

None of the integration points in the elements nearby the cut-out region reached the fracture criterion to represent the through-thickness shear crack at the non-impacted end of the bumper beam (see Figure 13(c)). Thus, no integration point data are presented from this region.

No attempt is made to compare the experimental images and numerically predicted deformation modes for test series B. This is because the numerical simulations failed to predict the deformation and fracture modes observed in the experimental tests.

For test series C, deformation shapes from the numerical simulation and experimental images are compared in Figure 16. As can be seen in Figure 16(a), the non-impacted longitudinal in the numerical simulations had a more dominant buckle than in the tests. Moreover, in the tests the upper hinge was developed close to the interface plate, and in the simulation it was predicted far away from the interface plate. This kind of overprediction of buckling in the simulations may be attributed to the lack of modelling initial imperfections in the extruded member. Progressive folds in the impacted longitudinal are compared in Figure 16(b). The number of lobes developed in the simulation and test is the same. However, the rupture in the folded compression flange and the webs of the bumper beam is poorly predicted in the simulations (Figure 16(c)), although some integration points in the elements reached the fracture criterion.

## ENERGY DISSIPATION

Numerical simulations make it possible to understand how the energy has been distributed in the system with the progress of deformation. The amount of energy dissipated

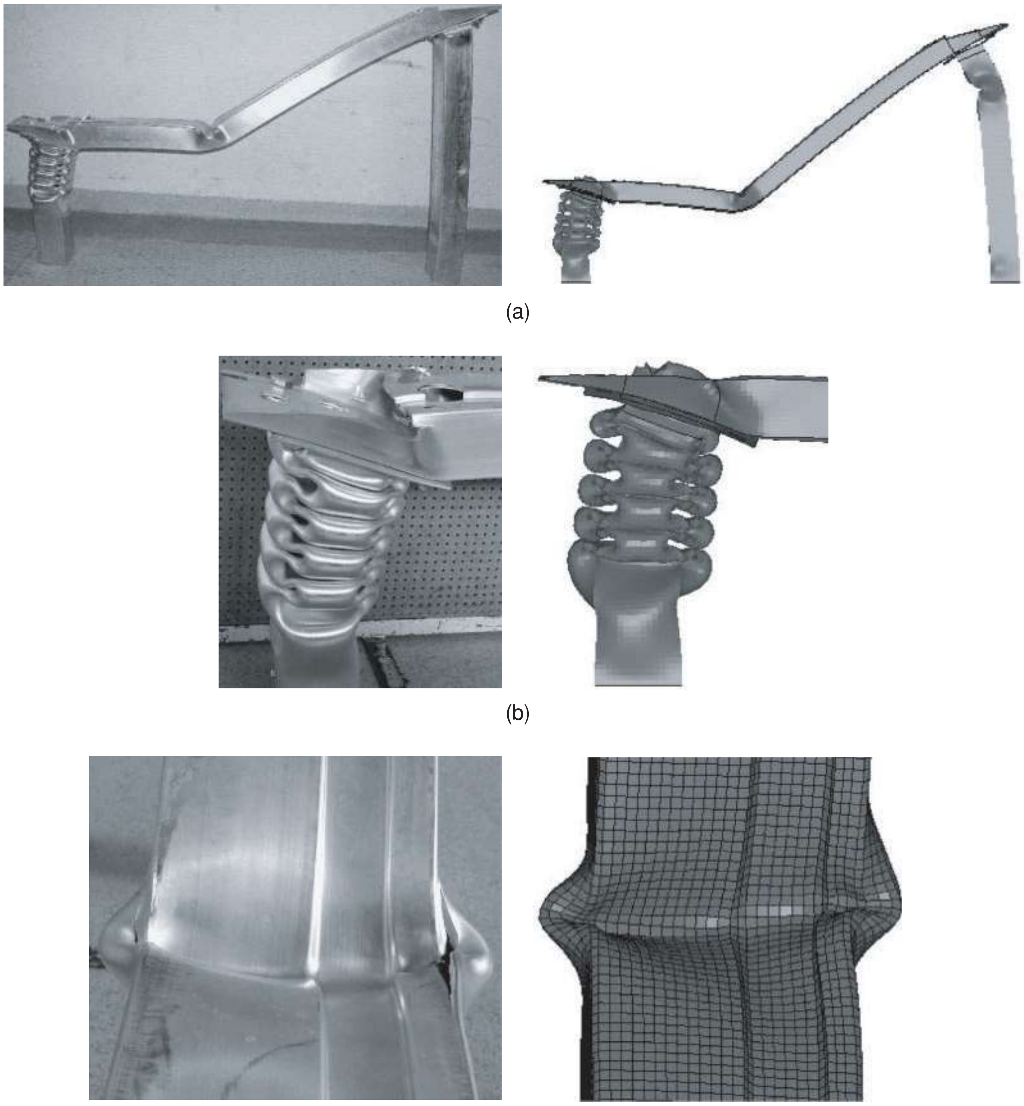

*Figure 16* Comparison of permanent deformation shapes of test specimen C1 [4] and that obtained from simulations with MAT-41(*CFS**) model.

through different parts of the bumper beam–longitudinal system when using the MAT-41(*CFS**) model is summarized in Tables 10–12 for test series A, B and C, respectively. Figure 17 shows the energy–deformation plots for all the components in the bumper beam–longitudinal system for test series A, B and C. The force–deformation curves from the numerical simulations are also shown on the top of the same figure.

For test series A and B, the energy dissipation in the impacted longitudinal started at a deformation of 100 mm. Prior to this deformation, the energy is dissipated in collapsing the bumper beam cross section at the impacted end. This point strongly supports the fact that in the experiments of test series A and B, the bumper beam collapsed before the buckling initiation in the impacted longitudinal started [4]. Thus, it is clear that the initiation of buckling in the impacted longitudinal has led to the high peak in the force–deformation plots for test series A and B. It can be concluded that this peak probably can be reduced by modelling initial geometric imperfections or by increasing the assumed length of the HAZ.

*Table 10* **Material internal energy for test series A**

| Part | Internal energy (kJ) | Percentage (%) |
|---|---|---|
| Impact energy | 39.7 | 100 |
| Bumper beam | 6.9 | 17.38 |
| Impacted longitudinal | 28.96 | 72.95 |
| Non-impacted longitudinal | 0.82 | 2.06 |
| Impacted interface plate | 0.98 | 2.46 |
| Non-impacted interface plate | 0.40 | 1.01 |

*Table 11* **Material internal energy for test series B**

| Part | Internal energy (kJ) | Percentage (%) |
|---|---|---|
| Impact energy | 39.7 | 100 |
| Bumper beam | 6.79 | 17.10 |
| Impacted longitudinal | 28.96 | 72.94 |
| Non-impacted longitudinal | 0.81 | 2.04 |
| Impacted interface plate | 0.99 | 2.49 |
| Non-impacted interface plate | 0.39 | 0.98 |

*Table 12* **Material internal energy for test series C**

| Part | Internal energy (kJ) | Percentage (%) |
|---|---|---|
| Impact energy | 39.7 | 100 |
| Bumper beam | 4.90 | 12.34 |
| Impacted longitudinal | 16.73 | 42.14 |
| Non-impacted longitudinal | 1.15 | 2.89 |
| Impacted interface plate | 0.35 | 0.88 |
| Non-impacted interface plate | 0.22 | 0.55 |

Contrary to other test series, the energy dissipation in the impacted longitudinal of test series C started at a deformation of 50 mm (see Figure 17). As the buckling in the impacted longitudinal started, the bumper beam cross section did not collapse completely and the high peak which was observed in other test series was not observed here.

The energy dissipation by the interface plate at the impacted end started at a deformation of 50 mm in test series A and B. This corresponds to 50% collapse of the bumper beam cross section. The energy dissipated by the non-impacted interface plate in test series A and B is 1% of the total impact energy, whereas in test series C the value is 0.5%. The energy dissipated in developing the plastic hinge(s) in the non-impacted longitudinal varies from 2.04% to 2.89% (see Tables 10–12). The lowest being in test series B, while the highest is in test series C. In the latter case the non-impacted longitudinal had two buckles.

The energy dissipated by the impacted longitudinal in test series A and B was the same with 73% (Tables 10 and 11). This shows that in the offset impacts the longitudinals are the key structural elements for dissipating the impact energy. Thus, the longitudinals deserve a closer look since they contribute to great percentage of the total energy dissipated. From Table 12, it is clear that the impacted longitudinal dissipated only 42% of the available impact energy for test series C. This is mainly due to the lower strength of the material [4].

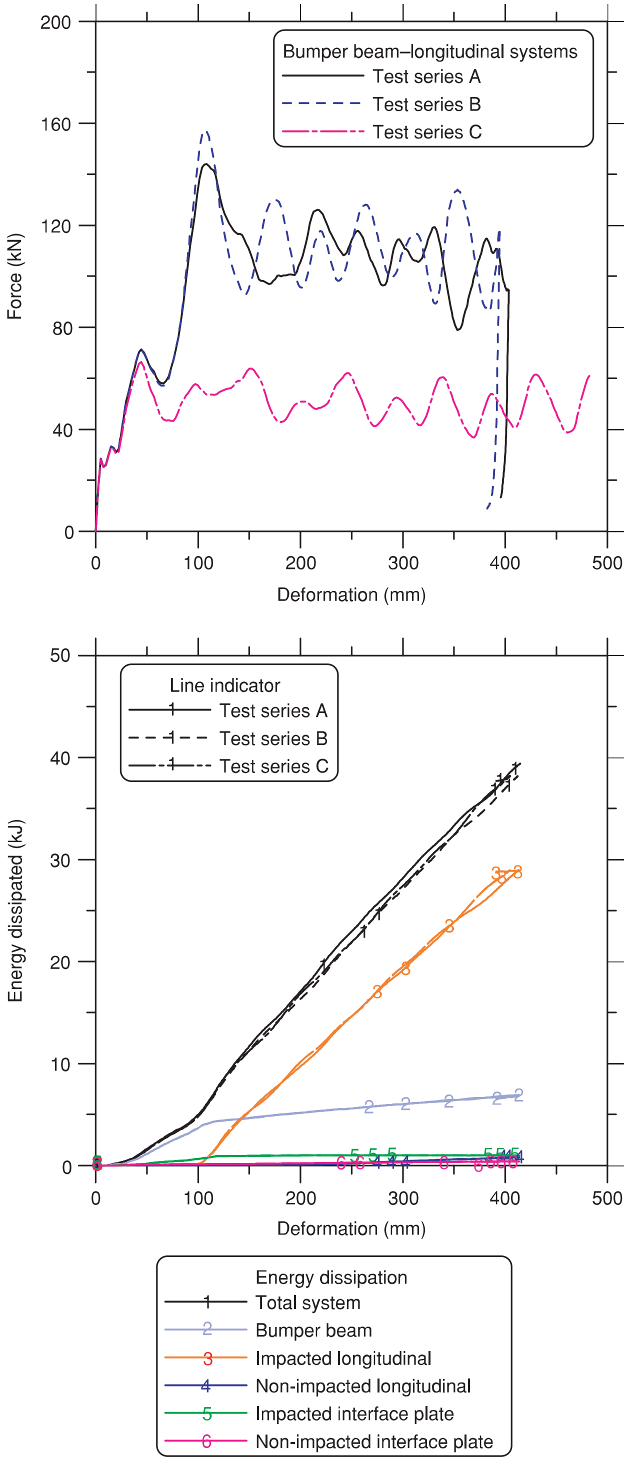

*Figure 17* Force–deformation plots, energy distribution with respect to deformation for test series A, B and C.

## SENSITIVITY STUDIES

Sensitivity studies have been carried out for test series A and C; the corresponding results are compared with a baseline model as well as with the tests. For the test series A, the material model that was discussed in the section 'Test series A', i.e. MAT-41(*CFS**), is taken as the baseline model. Whereas for test series C also the MAT-41(*CFS**) model (see the section 'Test series C') is considered as a baseline model. No sensitivity study was performed for test series B. The sensitivity studies included both the physical and numerical parameters. The physical parameters investigated were the strain-rate effects for test series A and C, the HAZ for test series A. The only numerical parameter

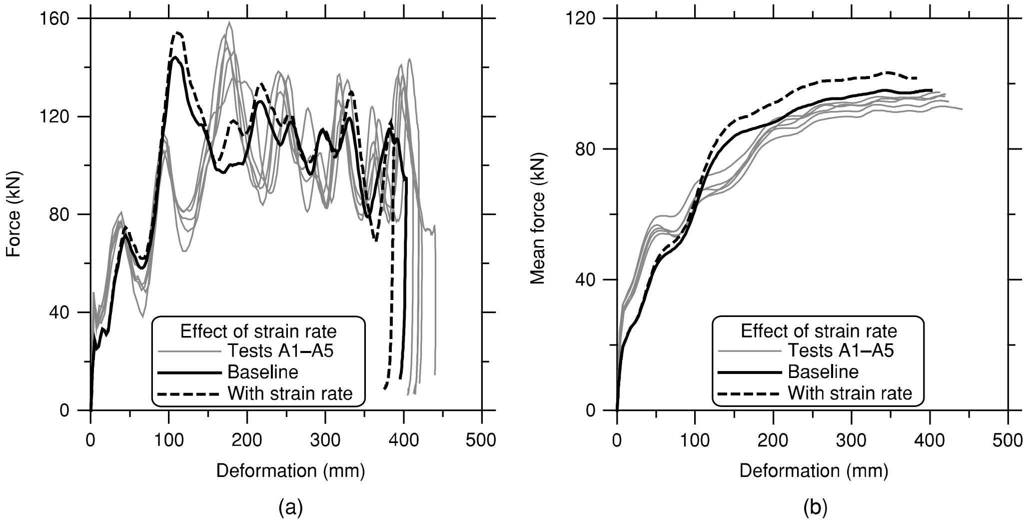

*Figure 18* Strain-rate effects on the response of test series A: (a) force–deformation and (b) mean force–deformation.

investigated was the adaptive meshing technique (for the prediction of fracture events in the bumper beam) for test series A.

### Strain-rate

The strength variation at different strain rates for the bumper beam (AA7108-T6) and the longitudinals (AA7003-T79) is discussed by Reyes *et al.* [7]. They observed that the strain-rate affects the flow stress of the materials for both alloys. The increase in material strength in the strain-rate ranging from $10^{-4}$ $s^{-1}$ to $10^{3}$ $s^{-1}$ is 15% for AA7108-T6 and 25% for AA7003-T79.

In the baseline model, the material is assumed to be strain-rate insensitive. Strain-rate effects are included in the constitutive model as explained in the section 'Strain-rate hardening'.

In the analysis of the dynamic plastic response of automobile bumper beam structures subjected to crash loading, strain-rate sensitivity effects may be important. Failure to account for such effects in the analysis may result in completely unrealistic results [17].

The numerical response of the bumper beam–longitudinal system when considering strain-rate effects (test series A) is compared with the baseline model and tests in Figure 18. The figure clearly depicts that with the consideration of strain-rate sensitivity the average force level increases. The deformation mode predicted in the numerical simulations for both cases, i.e. with and without consideration of strain-rate sensitivity, was the same, but the amount of deformation is less when strain-rate sensitivity is taken into account. In other words, this implies that the total impact energy of the impactor was absorbed over a smaller deformation which can also be noted from the mean force–deformation plot in Figure 18(b). The mean force predicted is higher for the system with strain-rate effects. From the simulations, it can be concluded that strain-rate effects are of importance and without the inclusion of these effects, the peak moments (and thus, peak decelerations) might be considerably underestimated (see Figure 18(a)).

For test series C, the predicted deformation mode of the system was close to that observed in the tests (except the buckle in the non-impacted longitudinal), but the mean force level was underestimated compared to the tests, see the section 'Test series C'. In the simulations with MAT-41(*CFS**), the strain-rate effects were neglected.

Enjalbert [18] performed material tests on AA6060-T6 and has shown that it has a small strain-rate sensitivity. Even though it is small, it may have an influence on the mean force level. Enjalbert [18] performed tensile tests on specimens cut from aluminium alloy 6060-T6 tube with 4.5 mm wall thickness in a hydraulic testing machine and in a 'split Hopkinson tension bar' similar to the programme reported by Reyes *et al.* [7]. Figure 19 shows the reported strain-rate sensitivity at different levels of plastic strain. As can be seen, there is small positive strain-rate sensitivity for AA6060-T6. Equation (8) was used to take strain-rate effects into account. The parameters are listed in Table 13.

The response of test series C, when considering the strain-rate sensitivity parameters for temper T6, is plotted together with the baseline model and tests in Figure 20. From the force–deformation and mean force–deformation plots in Figures 20(a) and (b), respectively, it is clear that there is some influence of strain-rate on the behaviour of the system. The mean-force level is increased with the inclusion of rate effects, and matches exactly with the tests at the final deformation.

### Heat-affected zone

In the FE-model (Figure 4), a length of 20 mm and a 30% reduction for the true stress–strain curve (Figure 6) were assumed in modelling of the HAZ. A case without the HAZ

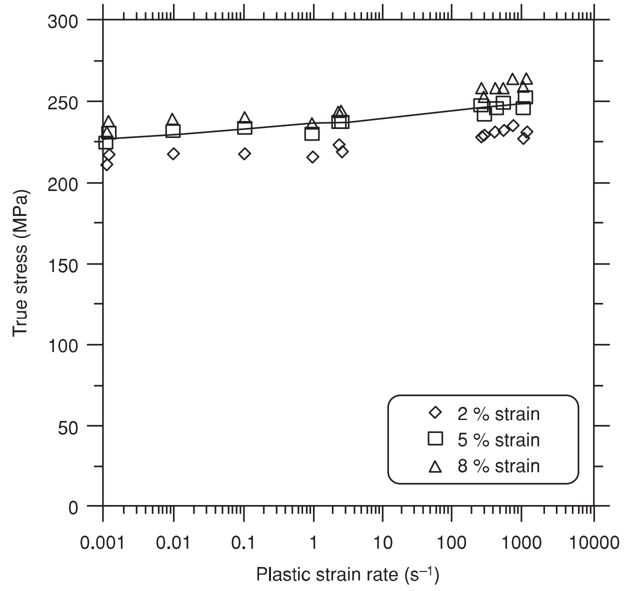

*Figure 19* Strain-rate sensitivity in AA6060-T6 [18].

*Table 13* **Strain-rate parameters for AA6060-T6**

| Alloy - Temper | $\dot{\varepsilon}_0$ (s$^{-1}$) | c (–) |
|---|---|---|
| AA6060-T6 | 1.0 | 0.001 |

was performed for test series A to study the influence of the HAZ (in the longitudinals) on the crash behaviour of the bumper beam–longitudinal systems.

Figure 21 shows the response of the bumper beam–longitudinal system with the baseline model, without the HAZ, but with and without strain-rate effects. The final permanent deformation shapes are compared in Figure 22.

When the HAZ was not modelled, the deformation mode changed. One would expect that when the HAZ was not modelled the force level in the system should increase, due to the increased stiffness of the longitudinals. On the contrary, a lower force level with increased permanent deformation was observed in the simulations (Figure 21(a)). Thus the mean force as well as the energy absorbed by the bumper beam–longitudinal system decreased (Figure 21(b)), when the rate effects were ignored. However, the behaviour was opposite when the rate effects were taken into consideration.

The reasons for such behaviour of the system are as follows: With the initiation of buckling in the impacted longitudinal in the baseline simulation, the deformation was concentrated in the soft zone, i.e. in the HAZ itself. The formation of a second buckle led to a rise in the force level at a deformation of 200 mm (see Figure 21(a)). When the HAZ was not modelled, however, a higher force was required to initiate the buckling in the impacted longitudinal. Thus the deformation was not concentrated, as in the baseline model, and simultaneously the buckling pattern was developed over the entire length of the longitudinal. This pattern helped in the easy formation of buckles with the progress of the deformation process. The above is also applicable when the strain-rate effects are taken into consideration. However, there was a much higher peak force in the simulations when the rate effects were considered.

A clearer progressive buckling mode developed in the impacted longitudinal when the HAZ was not modelled (Figures 22(b) and (c)), and the permanent deformation of the system increased without the rate effects. The predicted permanent deformation without the HAZ, but with rate effects, was close to the tests (see Figure 21(a)). When the HAZ was not modelled, it can further be seen that there are some rotational effects on the deformed end of the impacted longitudinal. On the other hand, no local buckle developed at the clamped end of the impacted longitudinal, which is in better accordance with the experiments.

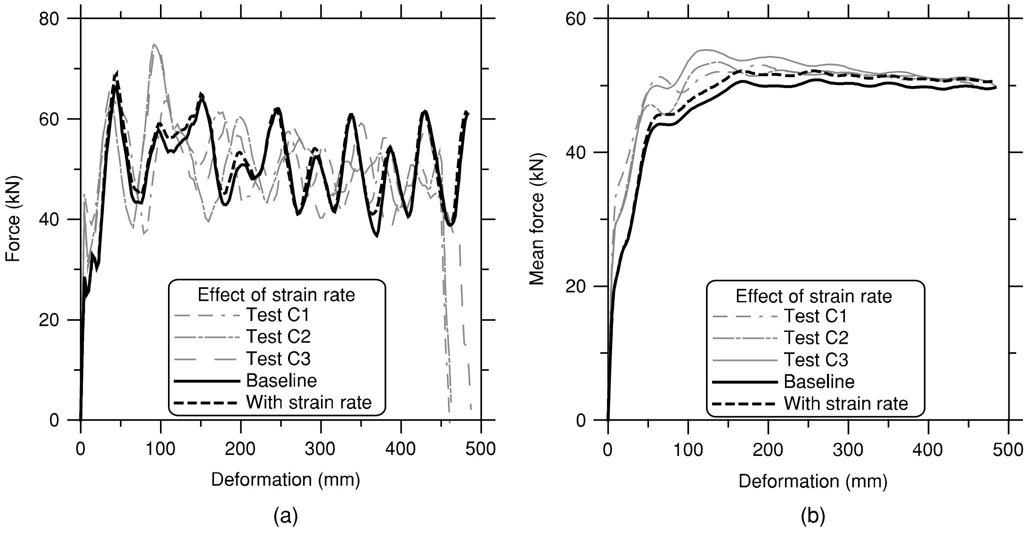

*Figure 20* Strain-rate effects on the response of test series C: (a) force–deformation and (b) mean force–deformation.

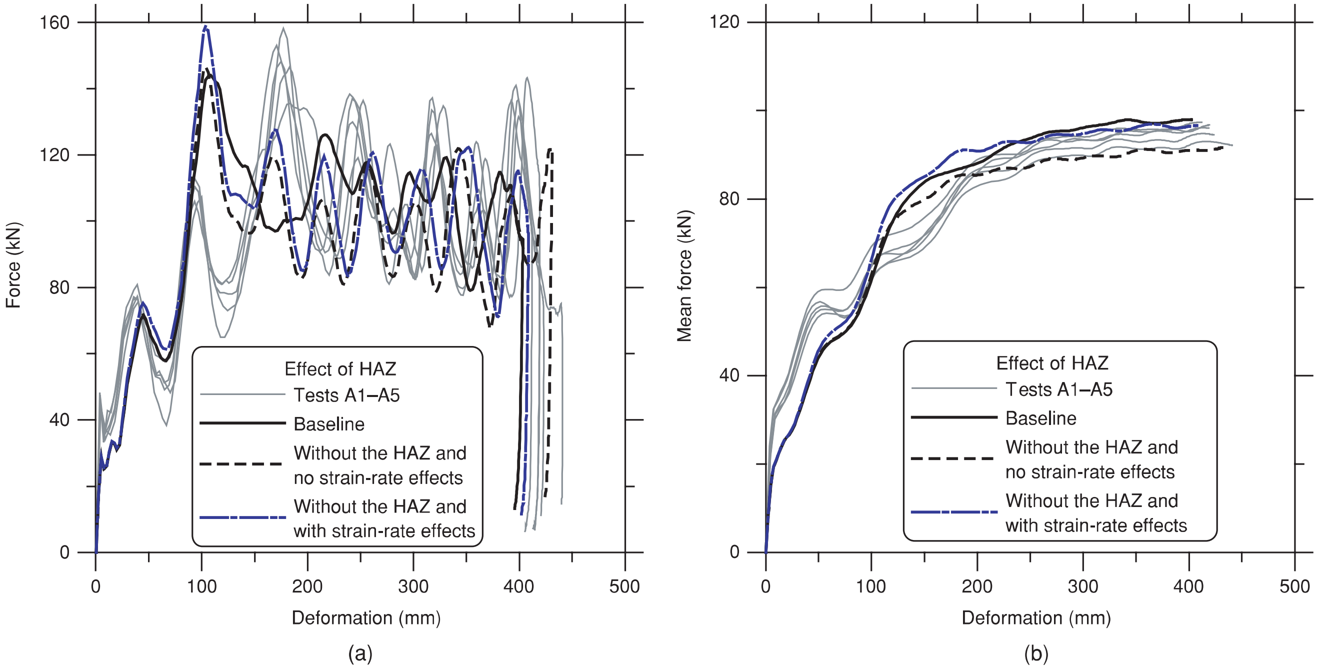

*Figure 21* Influence of HAZ on the crash behaviour of test series A: (a) force–deformation and (b) mean force–deformation.

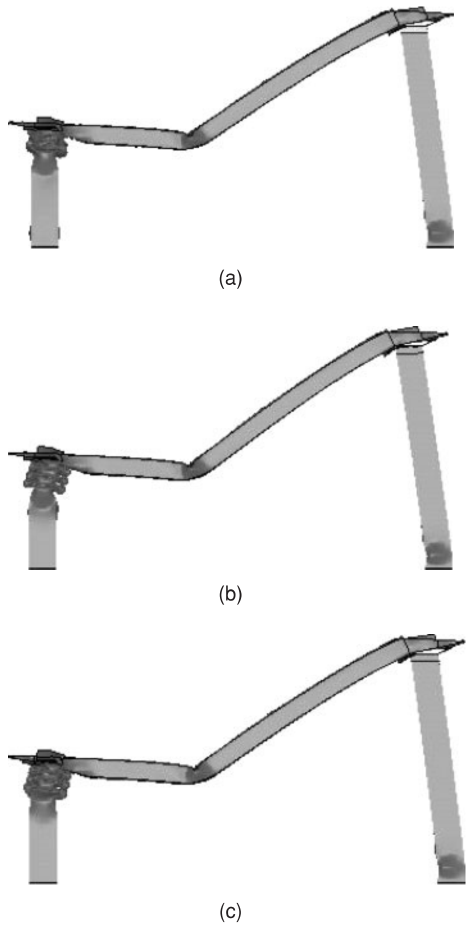

*Figure 22* Final deformation shapes of test series A from the simulations (a) with the HAZ (baseline model), (b) without the HAZ, no strain-rate effects and (c) without the HAZ, with strain-rate effects.

### Adaptive meshing

The basic reason for employing adaptive meshing was mainly to predict the fracture events at the non-impacted end and in the mid-section (i.e. bending failure in the webs and flanges) of the bumper beam (see Figure 13). It was assumed that the current element size ($5 \times 5$ mm$^2$) was too large and thus the reason why the simulations failed to predict the fracture. Hence, in order to predict these failure modes simulations with adaptive meshing were performed on the baseline model of test series A. The adaptive meshing was applied only for the bumper beam using the *CONTROL_ADAPTIVE card in LS-DYNA [3].

By default LS-DYNA utilizes an h-adaptivity for shell elements [3]. In the h-adaptive method, the elements are sub-divided into smaller elements whenever an error indicator shows that sub-division of the elements will provide improved accuracy. For the present simulations, the maximum refinement level is set to 2 and a thickness strain error indicator is used. The absolute shell thickness level below which adaptive re-meshing should begin is set to 3.3 mm. This means that whenever the adaptive re-meshing thickness criterion is satisfied the element is divided into four sub-elements. More details about the use of adaptive meshing can be found in Hallquist [3].

As mentioned earlier, the longitudinal and the interface plate were MIG welded in order to connect the longitudinal to the back face of the bumper beam. Because of the welding some extra material is added in the form of a fillet in the welded section. To represent this material, the thickness of selected rows of elements in the HAZ is assigned an increased thickness. The increased thickness was assigned to the two rows of elements in the HAZ closest

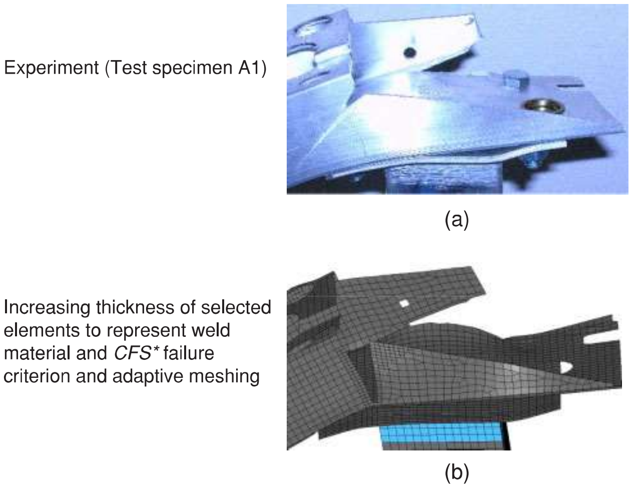

*Figure 23* Comparison of fracture events at the non-impacted end of the bumper beam, experiment versus numerical simulations: (a) Experiment (test specimen A1) and (b) increasing thickness of selected elements to represent weld material and *CFS** failure criterion and adaptive meshing.

to the interface plate and two rows in the interface plate (Figure 4). Only when the thickness increased 2.5 times, a change in the fracture mode was observed [14].

Figure 23 reveals that the use of adaptive meshing helps in predicting a clearer fracture path due to the sub-division of the elements in critical areas. It was observed that the bending failure in the mid-section of the bumper beam was not captured when employing the adaptive meshing technique. Thus, no images of bending failure in the bumper beam are presented.

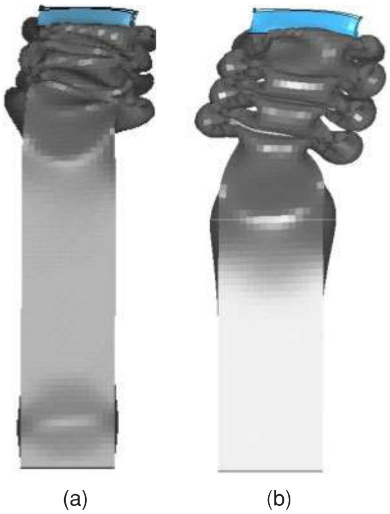

*Figure 25* Permanent deformation shapes of the impacted longitudinal when increasing the thickness of selected elements to represent weld material addition (a) without and (b) with adaptive meshing of the bumper beam.

The force–deformation and mean force–deformation plots are compared with the baseline model in Figure 24. Up to the formation of the first two lobes in the impacted longitudinal, the adaptive meshing had no influence. The curves with and without adaptive meshing started to deviate at a deformation of 150 mm. The system without adaptive meshing had a higher peak force, which was almost the same height as the initial peak force. Whereas the system with adaptive meshing the force level was lower than the initial peak. This is due to the erosion of the

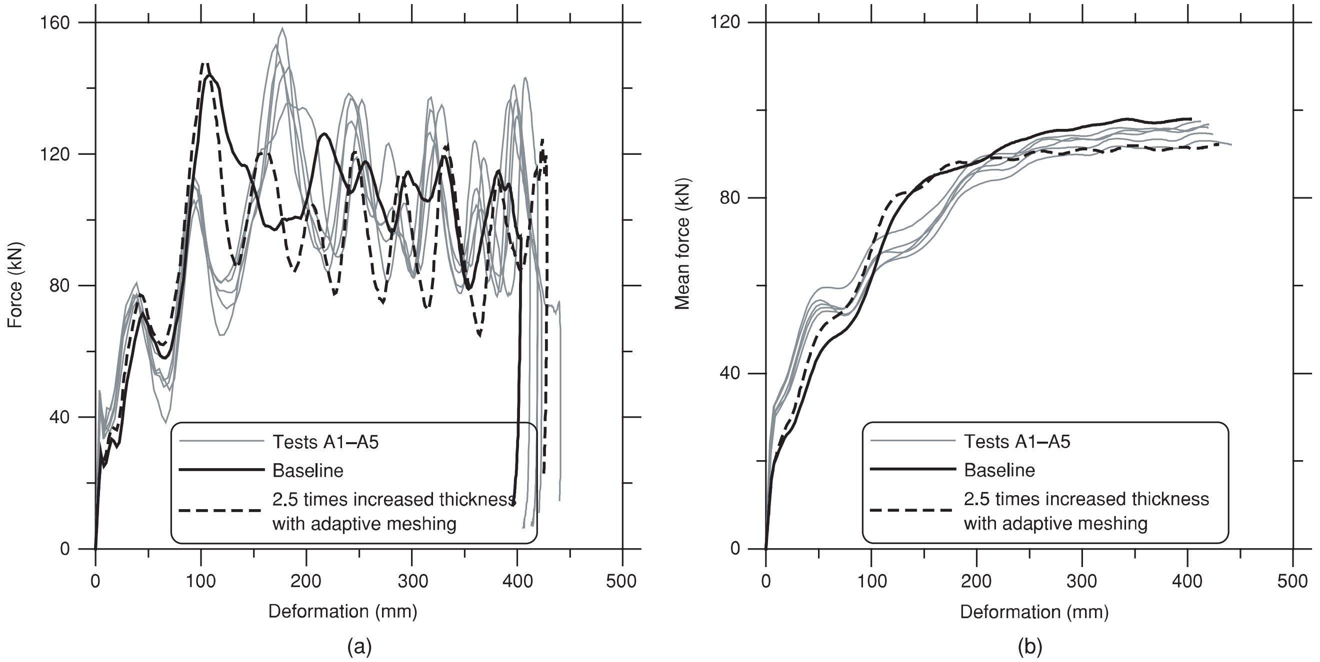

*Figure 24* Influence of increasing the thickness of selected elements to represent weld material addition and also use of adaptive meshing (a) force–deformation and (b) mean force–deformation.

elements at the intersection of the lower flange and the web of the bumper beam.

Simultaneously, re-meshing took place near the cut-out region of the bumper beam. The mean force of the system decreased considerably (Figure 24(b)), compared to the baseline model without adaptive meshing. The deformation mode of the impacted longitudinal has changed from a mixed mode to a progressive folding mode with the application of adaptive meshing, when modelling them as close as possible to reality, i.e. increasing the thickness of the selected rows of elements in the HAZ to represent the fillet material addition due to welding (see Figures 25(a) and (b)).

## CONCLUSIONS

In the present paper, numerical simulations were performed on bumper beam–longitudinal systems subjected to 40% offset impact and compared with experimental results [4] for each test series A, B, and C. The influence of the yield criterion on the crash performance of the bumper beam–longitudinal system was studied using the non-linear FE-code LS-DYNA. The results revealed that for a given amount of deformation, the predicted energy dissipation was higher with the currently available material models in LS-DYNA [3] than with the user-defined material model (MAT-41; including state-of-the-art anisotropic plasticity, associated flow rule, an isotropic strain and strain-rate hardening rule as well as ductile fracture criterion).

Simulation results reveal that proper modelling of the HAZ is required, and the strain-rate effects should be taken into account. Application of adaptive meshing technique along with a fracture criterion helped in predicting similar fracture modes as in the tests for the bumper beam. This also gave a change in deformation mode of the impacted longitudinal.

In the present work, the simulation results presented are based on a geometry of the bumper beam that is generated from forming simulations [14]. Thus, in the bumper beam model, the thickness changes resulting from the forming process have been taken into consideration, while the process effects on the material level have not been included. In the further work, the process effects will be incorporated into the current FE-model to study the downstream effect of the manufacturing process on the crash behaviour of bumper beam–longitudinal systems and in prediction of fracture in the critical areas.

## ACKNOWLEDGEMENT

The present work has been carried out with financial support from Research Council of Norway through the Strategic University Programme (SUP).

## REFERENCES

1. O-G Lademo, T Berstad, M Eriksson, T Tryland, T Furu, O S Hopperstad and M Langseth, 'A model for process-based crash simulation', *Int J Impact Eng*, 2006.
2. O-G Lademo, T Berstad, O S Hopperstad and K O Pedersen, 'A numerical tool for formability analysis of aluminium alloys, Part I: Theory', 10th int conf *Metal Forming*, Kraków, Steel Grips, 2004.
3. J O Hallquist, *LS-DYNA Keyword User's Manual v 970*, Livermore Software Technology Corporation, Livermore, CA, 2003.
4. S Kokkula, M Langseth, O S Hopperstad and O-G Lademo, 'Offset impact behaviour of bumper beam–longitudinal systems – experimental investigations', *Int J Crashworthiness*, 2006 **11**(4) 299.
5. T Belytschko, W K Liu and B Moran, *Nonlinear Finite Elements for Continua and Structures*, West Sussex, Wiley, 2000.
6. J Lemaitre and J-L Chaboche, *Mechanics of Solid Materials*, Cambridge, UK, Cambridge University Press, 1990.
7. A Reyes, O S Hopperstad, O-G Lademo and M Langseth, 'Modeling of textured aluminium alloys used in a bumper system: Material tests and characterization', *Comput Mater Sci*, August 22, 2005.
8. H Aretz, 'Applications of a new plane stress yield function to orthotropic steel and aluminium sheet metals', *Modelling Simul Mater Sci Eng*, 2004 **12** 491–509.
9. J R Yeh, T L Summe and D C Seksaria, 'The development of an aluminum failure model for crashworthiness design', conf *Crashworthiness, Occupant Protection and Biomechanics in Transportation Systems*, New York, ASME, 1999.
10. A Reyes, O S Hopperstad, A G Hanssen and M Langseth, 'Modeling of material failure in foam-based components', *Int J Impact Eng*, 2004 **30** 805–834.
11. T Berstad, O-G Lademo, K O Pedersen and O S Hopperstad, 'Formability modeling with LS-DYNA', 8th *LS-DYNA International Users Conference*, Detroit, MI, 2004.
12. R Hill, *The Mathematical Theory of Plasticity*, Oxford, UK, Clarendon Press, 1950.
13. True*Grid*® *Manual*, version 2.1.0, Livermore, CA, XYZ Scientific Applications, Inc., 2001.
14. S Kokkula 'Bumper beam–longitudinal system subjected to offset impact loading. An experimental and numerical study', PhD Thesis, Department of Structural Engineering, Norwegian University of Science and Technology, Trondheim, 2005.
15. 'prEN 199 9-1-1, Eurocode 9: Design of aluminium structures, Part 1.1: General structural rules', CEN, rue de Stassart 36, Brussels, 2004.
16. S Kokkula, O S Hopperstad, M Langseth and O-G Lademo, 'Explicit and implicit analysis of beams subjected to impact loading with axial restraints', 16th *Nordic Seminar on Computational Mechanics in Combination with the Pål Bergan Anniversary Seminar*, Trondheim, Tapir Uttrykk, 2003.
17. R C Shieh 'Strain rate sensitivity effects on crash response and dynamic yield moment formulas for crash prediction of automobile bumpers', 16th *Structures Structural Dynamic and Material Conference*, Reston, VA, American Institute of Aeronautics and Astronautics, 1975.
18. P Enjalbert, 'Strain-rate sensitivity of aluminium alloy AA6060-T6', MSc Thesis, Department of Structural Engineering, Norwegian University of Science and Technology, Trondheim, 2003.

doi:10.1533/ijcr.2005.0106